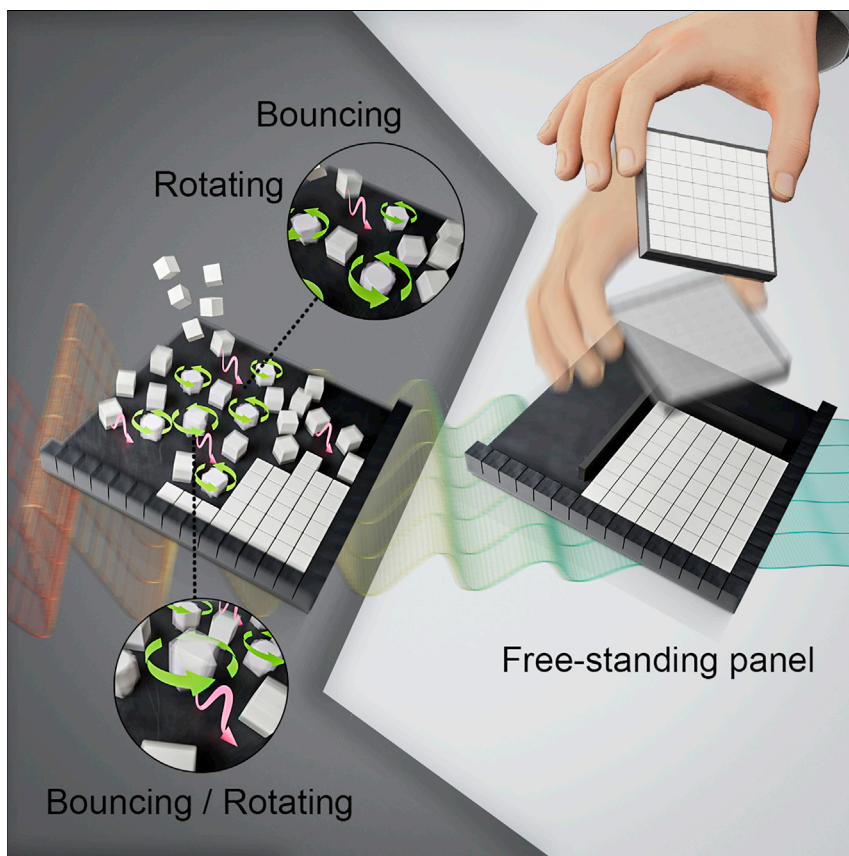


Article

Vibration-driven fabrication of dense architected panels



Block-based architected materials are made by polyhedral blocks and joined by weaker interfaces and can display remarkable mechanical performance. The widespread use of these materials is limited by fabrication challenges. A rapid and low-energy pathway can be self-assembly using vibration and gravity. We showed that the cubic grains can be self-crystallized using this technique and used as a free-standing architected component. We assessed the mechanics and physics underlying this process to provide guidelines for optimizing the assembly of complex materials.

Aram Bahmani, J. William Pro,
Florent Hannard, Francois
Barthelat

francois.barthelat@colorado.edu

Highlights

Vibration-assisted assembly is an efficient fabrication method for granular matter

Vibrations can crystallize polyhedral grains into large 2D panels

Vibration amplitude and frequency are critical parameters in the assembly process

The states of blocks are characterized into three regimes and two phase transitions

**Understanding**

Dependency and conditional studies on material behavior

Article

Vibration-driven fabrication of dense architected panels

Aram Bahmani,¹ J. William Pro,¹ Florent Hannard,^{1,2} and Francois Barthelat^{1,3,4,*}

SUMMARY

Self-assembly at the macro-scale is a promising pathway for fabrication, but the assembly process and mechanisms are still poorly understood. We examine the vibration-induced assembly of hard cubic grains as a potential route for the rapid fabrication of architected materials and structures. We performed assembly experiments with various combinations of vibration amplitudes and frequencies to map the different states of the system. The results show that the acceleration normalized by gravity cannot fully capture the phase transitions or the mechanisms governing cubes packing and that amplitude and frequency must be considered independently. We used discrete element modeling to duplicate experiments and then single-grain models to find the effective mechanisms involved in the packing and phase transition of cubes. Both cube rotation and bouncing govern packing, while bouncing has an additional role in the phase transition. These findings provide guidelines for the assembly of complex materials, for example, topologically interlocked materials.

INTRODUCTION

Novel and innovative fabrication methods have recently been proposed for the fabrication of complex materials with highly tuned architectures, morphological features, and interfaces at meso-scale (between grain size and the whole component).^{1–3} Examples of these methods include freeze casting,^{4,5} 3D printing,² laser engraving,^{6,7} and centrifugation.⁸ Some of these fabrication methods were specifically developed to duplicate natural materials, such as nacre or bone, which can be interpreted as complex assembly of hard building blocks bonded by softer biopolymers (proteins and/or polysaccharides).⁹ Interestingly, the concept of building-block-based materials joined by weaker interfaces is also used in topologically interlocked materials,¹⁰ which can turn brittle components like ceramics or glasses into tough, impact-resistant systems^{11,12} or materials with tunable mechanisms, precise structural responses, and functionalities not ordinarily found in monolithic solids.^{12–18} The assembly of the building blocks presents special challenges. Example of the proposed methods include pick-and-place assembly, parallel assembly, magnetic assembly, 3D printing, and segmentation.^{8,18} A promising pathway to fabricating these materials is self-assembly.^{9,19} Self-assembly has importance in chemistry, biology, and engineering, among other fields.^{20–24} The majority of theoretical and experimental studies on self-assembly, however, focuses on nano- and microscale structures, for example, dense packing of colloids.^{25–29} Several numerical methods, including Monte Carlo and molecular dynamics, have also been used to study phase transitions and crystallization in thermal equilibrium systems.^{30–33} At this point, it is useful to highlight analogies between building-block-based materials and granular materials. Both systems are athermal and far from thermodynamic

Progress and potential

Architected materials are an emerging class of material with unusual structural behavior, which can surpass the performance of traditional materials. Fully dense architected materials are based on blocks that must be assembled into materials and structures, which represents challenges that hamper the broader application of these materials. An underused yet promising fabrication pathway is vibration-assisted assembly at the macro-scale, a process where individual building blocks are organized into a pre-designed and ordered structure. Understanding and optimizing the vibration+assisted assembly of these material systems can be used as guidelines in the physics and mechanics of other complex granular media. We propose a vibration-induced assembly route enabling scalable, rapid, low-energy fabrication of these materials. The self-assembly applications of these materials include armor and protective suits; transformable and freeform structures; and biomedical, aerospace, and astronautics materials.

equilibrium,^{34,35} and frictional and inertial forces are prominent. Interestingly, grains can be assembled or “crystallized” using mechanical stimuli, such as shearing or vibrations.^{35–45} However, most reports on granular crystallization have focused on the packing and phase transition of spherical grains,^{34–36,42–45} and much fewer reports have considered the assembly of polyhedral building blocks.^{37–41,46–48} Several mechanisms in packing and phase transitions of granular matter have been described in the literature.^{37–47} For example, the intensity of the mechanical excitation has often been described with a single parameter: the maximum acceleration normalized by the gravitational acceleration,^{49,50} but the details of the mechanisms involved in each regime have yet been established, especially for cases where the grains (or building blocks) are non-spherical. A better understanding of the mechanisms that govern vibration-induced assembly of non-spherical blocks is therefore needed so that method can be used for the large-scale fabrication of complex materials. In this work, we examine a vibration-induced self-assembly method to rapidly fabricate dense segmented macro-scale materials and/or structures based on meso-scale cubic grains. We explore the effects of vibrations on the possible states of granular hard cubes (including crystallization), with particular attention to the decoupling of vibration amplitude and frequency responses. In parallel, we duplicate the experiments using discrete element modeling (DEM), and we use DEM to predict and study the physics and mechanics underlying vibration-induced assembly of architected panels.

RESULTS AND DISCUSSION

Experiments

The goal of the experiments was to explore the vibration-induced assembly, or “crystallization,” of a 2D panel from stiff, cubic building blocks or “grains.” We focused on cubical blocks for this study because they are one of the simplest regular volumes that can tessellate a thick panel. While more advanced geometries can generate interlocking between the blocks, many of these geometries are actually variations of the cubical shape (truncated tetrahedra and tetrahedra¹²). Our objective was to work at the millimeter scale to ensure that the granular systems were athermal. Then, blocks about 5 mm in size were chosen because they are relatively easy to fabricate with a high geometrical control. We fabricated 4.8 × 4.8 × 4.8 mm cubes of calcium sulfate using a replica-casting method (described in Mirkhalaf et al.¹²). Calcium sulfate (also known as gypsum or plaster of Paris) is a ceramic that is relatively easy to work with because it can be formed and cast at room temperature. In addition, the interpretation of the results and comparisons with models is made easier by the absence of plastic yielding and relatively high hardness compared with polymers. For this work, we used the strongest type of calcium sulfate plaster (type V from Suprastone, Kerr Dental, Charlotte, NC, USA) with an optimized casting method that maximizes density and strength.⁵¹ The density (ρ) of our calcium sulfate was 2.3 g/cm³, the measured modulus $E = 11$ GPa, and the measured compressive and tensile strength 90 and 31 MPa. Finally, we chose calcium sulfate because the lowest resonant frequency of the blocks (approximated by $(\pi/l)\sqrt{E/\rho} \sim 1.43$ MHz) was orders of magnitude higher than the frequency of the vibrations we used for assembly (order of 1 kHz). The modulus and density of the material also govern the timescale of the contact interactions,⁵² which we wanted to be much smaller than other characteristic timescales in the problem. The experimental setup used to assemble the calcium sulfate cubes consisted of a polymethylmethacrylate (PMMA) square platform with walls (5 mm high) on each side, glued onto a voice coil with either a 45 W/60 W RMS/peak power capacity and a frequency response range of 45 Hz–4 kHz or a 120 W/240 W RMS/peak with a frequency

¹Department of Mechanical Engineering, McGill University, Montreal, QC H3A 0C3, Canada

²Institute of Mechanics, Materials and Civil Engineering, UCLouvain, Louvain-la-Neuve, Belgium

³Department of Mechanical Engineering, University of Colorado, 427 UCB, 1111 Engineering Drive, Boulder, CO 80309, USA

⁴Lead contact

*Correspondence:
francois.barthelat@colorado.edu
<https://doi.org/10.1016/j.matt.2022.01.002>

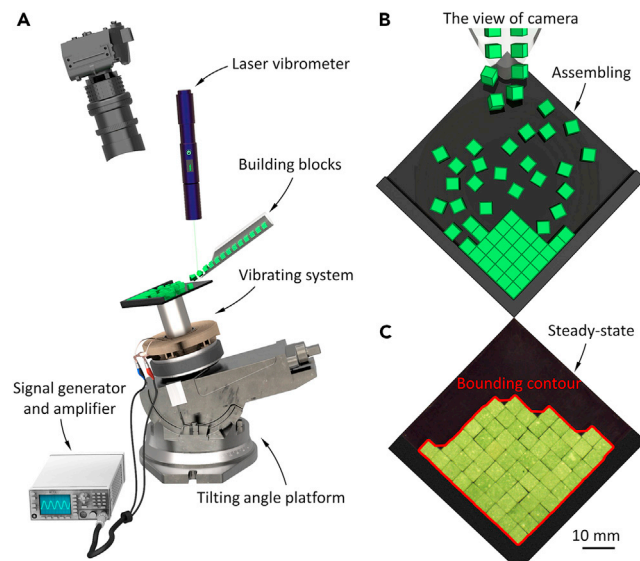


Figure 1. Experimental setup for the vibration-driven assembly of granular blocks

(A) Schematic of the vibration-induced self-assembly process, which is integrated with a high-speed camera and laser vibrometer. An assembly platform is glued on a voice coil, and the voice coil is fixed on a tilting angle platform and controlled by a signal generator and amplifier. (B) Hard cubes are randomly dropped on the tilted platform while it is vibrating. (C) Example of the image acquired from the experiments, overlaid with the bounding contour used to measure the steady-state packing factor.

response range of $F_0 \sim 1$ kHz (depending on which particular range of amplitudes and/or frequencies we explored in the experiments). The voice coil assembly platform was mounted on a tilting angle platform set to an angle of 10° directed along a direction aligned with the diagonal of the assembly platform (i.e., the lowest point of the platform was a corner of the platform). A laser vibrometer was used to calibrate the amplitude and frequency of the platform, and a high-speed camera was used to monitor the trajectory of the cubes during assembly. We explored the assembly response of the cubes subjected to a broad range of amplitude (1–100 μm) and frequency (10–1,000 Hz). Sixty-four cubes were fed onto the vibrating platform in a way that was continuous but with random time intervals (0.1–1 s) for the drops and landing spots (Figure 1). The tilt of the platform and the friction were such that the cubes did not move without vibrations.

Figure 2 shows an example of a successful assembly where we used image analysis to track individual cubes. The cubes moved toward the lowest corner of the platform from the combined action of vibrations and gravity. The evolution of packing efficiency (Figure 2D) was measured at each video frame by computing the packing factor, which we measured using image analysis: the images were first binarized and then the boundary and projected top surface area of cubes were measured by the sum of white pixels area. We defined the steady-state packing factor as the sum of the projected top surface area for each cube divided by the bounding contour area (Figure 1), which is the closest outer boundary of the assembly of cubes. The bounding contour was computed using a “boundary” function similar to a convex hull function but allowing for concave contours that could closely match the domain of the cubes. For this study, we focused on the packing factor of the assembly, measured once all 64 cubes were dropped and once a steady state (i.e., the cubes did not move anymore) was reached in the system. A broad range of combinations

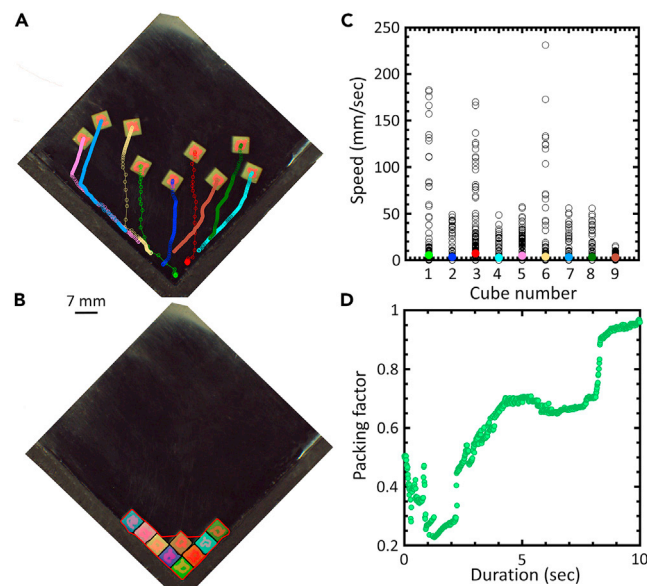


Figure 2. Example of results obtained on nine cubes dropped on a vibrating platform ($A = 10 \mu\text{m}$ and $f = 600 \text{ Hz}$)

(A) Trajectories of individual cubes by video recording and tracking the trajectory; (B) packed position of each cube; (C) instantaneous and average (filled color markers) speed of each cube; (D) evolution of packing factor versus duration of the vibrations.

of vibration amplitude and frequency was explored experimentally. For each combination of parameters, we repeated the experiment five times, and we computed an average packing factor from these experiments. The results were quite repeatable, and the deviation from the mean never exceeded 5% of the mean value, indicating that the system at steady state is not dependent on the initial conditions and therefore memoryless. In addition, [Figure 2](#) shows that, while the cubes have different trajectories and speeds, their average speed is almost equal, which suggests a common underlying mechanism driving their phase transition.

Depending on the vibration parameters for the platform, the cubes did not always assemble in a crystalline structure. We identified three main regimes for this system ([Figure 3](#)): at low vibration amplitude and/or frequency, the cubes did not move on the platform. In this “static” regime, the applied energy originating from vibrations was not sufficient to overcome frictional forces. At higher amplitude and/or frequency, the cubes bounced on the surface, which overcame friction and enabled more mobility. The general trajectory of the cubes was towards the lowest corner of the assembly platform, where they assembled into a 2D crystal. At higher combinations of amplitudes and frequencies, the system entered a “fluttering” regime, where the cubes bounced indefinitely in a chaotic fashion that precluded assembly. [Figure 3A](#) shows an experimental map of these different regimes as a function of a normalized frequency $f\sqrt{l/2g}$ and amplitude $2A/l$, where f is applied frequency, l is the size of cubes (edge length), g is the gravitational acceleration, and A is the vibration amplitude. The size of the block is an important parameter for vibration-induced assembly. For this reason, the vibration amplitude and the frequency were normalized using the size of the blocks l as the characteristic length. A color-map in the assembly region represents the measured packing factors for the assembly at steady state. Within this region, the packing factor increased progressively as amplitude and/or frequency was increased from the static-packing transition line

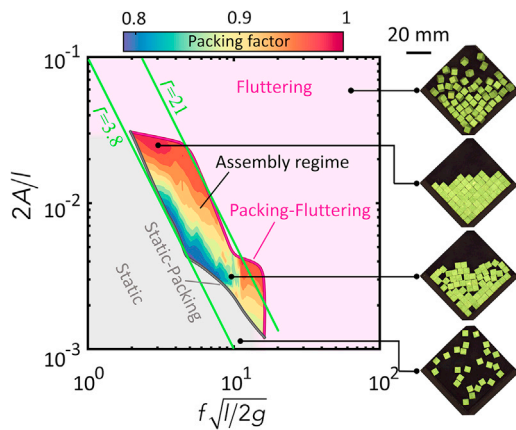


Figure 3. Experimental phase diagram showing the different states of the cubes as a function of dimensionless frequency and dimensionless amplitude

This map shows three main regimes: static; packing (contoured region showing final packing factor); and fluttering. The two green lines show the predictions from fitted relative acceleration models.

and reached a maximum of 1 (i.e., perfect packing) near the packing-fluttering transition line. The assembly process can be interpreted as a competition between vibration of the platform and friction between the blocks and the platform. For example, we expect that decreasing friction between cubes and the platform can shift the static-packing phase transition toward lower amplitudes and frequencies. Figure 3 also shows snapshots of the cubes at each regime.

The packing of granular matter subjected to vibrations has often been predicted as a function of dimensionless relative acceleration $T = A\omega^2/g$ ($\omega = 2\pi f$ and A is the vibration amplitude),^{40,49,50} where there is an “irreversibility point,” after which the packing factor was led to the steady-state condition.^{40,49,50} We fitted this model to our experiment, which predicted a critical acceleration for the static-packing boundary at $T = 3.8$ and for the packing-fluttering boundary at $T = 21$. However, these empirical values have no obvious physical significance, and the model did not capture the entire static-packing and packing-fluttering phase transition lines. These two phase transitions do have two different slopes, implying that there could be a distinctive mechanism governing each boundary. T also depends on the shape of the grain and experimental protocol, making this model inadequate for assessing the individual effect of amplitude and frequency on the phase transition and packing regimes.^{40,49,50} For example, Jaeger and coworkers reported $T \approx 3$ for spherical beads,^{49,50} while Neudecker et al.⁴⁰ reported various values ($T \approx 1.5$ –5) for tetrahedra. These values are empirical, and therefore, the relative acceleration model provides limited insight into the mechanics of assembly.

Discrete element modeling

For a better understanding of the assembly process, we used DEMs with the open-source C++/Python DEM solver Granoo, which is particularly well suited to the modeling of polyhedral grains.^{53,54} The parameters for the DEM simulations were taken directly from the experiments: the cubes were $4.8 \times 4.8 \times 4.8$ mm with modulus 11 GPa and mass density (ρ) 2.3 g/cm^3 , and the PMMA platform had a modulus of 3 GPa. A contact model that explicitly captures surface roughness was not used here. Rather, we assumed a standard Coulomb friction model. The contact model used in DEM simulations is linear and is based on the Gilbert-Johnson-Keerthi (GJK)-expanding polytope algorithm (EPA).^{55,56} This algorithm detects collision and computes penetration distance between colliding blocks, from which a contact force is computed. Here, we used a linear contact model where the contact is governed by a single contact stiffness, which is acceptable for intermittent contacts (this

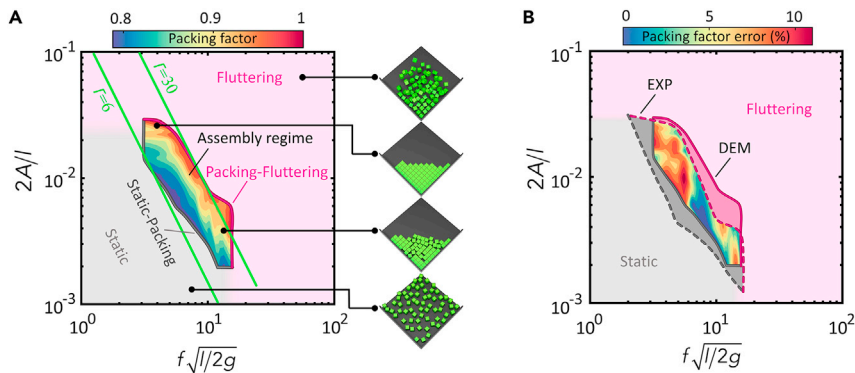


Figure 4. Assembly map predicted by DEM and compared with experiments

(A) DEM phase diagram showing the different states of the cubes as a function of dimensionless frequency and dimensionless amplitude. This map shows three main regimes: static; packing (contoured region showing final packing factor); and fluttering. The two green lines show the predictions from fitted relative acceleration models.

(B) Comparisons between experimental and DEM assembly maps are shown; the contoured region shows the percent error between experimentally measured packing factor and packing factor predicted from DEM simulation.

approximation of the contact also led to good agreements with the experiments). We measured the coefficients of friction using the ASTM D1894 standard. The cube-on-cube static and dynamic friction coefficients were 0.4 and 0.33, and the cube-on-platform static and dynamic friction coefficients were 0.38 and 0.27. To measure contact stiffnesses, we compressed a cube located on another cube or a PMMA plate and then measured the slope of linear force-deflection responses. These experiments gave cube-on-cube contact stiffness of 150 kN/mm and a cube-on-platform contact stiffness of 700 kN/mm. To measure the coefficient of restitution (CR), we simply dropped a cube vertically from a calibrated height onto a calcium sulfate or PMMA plate and then measured the bouncing height by a high-speed camera. These experiments revealed $CR = 0.3$ for cube on cube and $CR = 0.4$ for cube on platform. The coefficient of restitution was then calculated by $(\text{bounce height}/\text{drop height})^{0.5}$.⁵⁷ We first used our DEM models to compare with the experiments for validation. Sixty-four $4.8 \times 4.8 \times 4.8$ mm cubes were randomly generated and dropped onto a vibrating platform with a tilt angle of 10° . The system was subject to gravity and to a sinusoidal displacement applied vertically to the rigid platform. The duration for each simulation was 100 s—enough time to capture static, steady-state packing and fluttering regimes for any applied amplitude-frequency responses. The numerical time step was small enough to stable and converge the dynamic explicit solution. A broad range of combinations of vibration amplitude and frequencies was applied in the simulations, and the steady-state packing factor was measured using the same method as in experiments. Figure 4A shows the DEM-generated map of the different regimes as a function of vibration amplitude and frequency. The average packing factor in the DEM models was repeatable and memoryless, with a deviation of the packing factor of less than 10% across five different initial conditions for the cubes. Figure 4A also shows snapshots of the cubes in the DEM models at each regime. The contours represent the variation of the steady-state average packing factor. The highest packing factor region (i.e., 1) is in low-range frequencies and/or higher range amplitudes, an observation that is consistent with the experiments. Figure 4B overlays the assembly map predicted by DEM with the assembly map measured experimentally. There is good overall agreement between the two contours, although the DEM simulation

slightly overestimates the combinations of amplitudes and frequencies required to achieve assembly. [Figure 4B](#) also displays the error between experimental and DEM packing factors, which remains within about 10%.

In the following section, we sought mechanics-based models for the interaction of single grains with the substrate to gain a more fundamental understanding of the assembly process. The findings can inform more sophisticated models for the transitions and assembly of the granular system and in turn be used to optimize the material assembly process.

Bouncing of individual grains

The assembly process and [Figure 2](#) suggest that the bouncing of individual cubes can be a key mechanism to overcome friction and enable the motion of cubes on the assembly platform. Therefore, we considered a model based on the bouncing of one particle on the platform, with critical bouncing height and critical bouncing time as potential criteria for the phase-transition lines in the assembly process. Predicting the bouncing height and time of a particle on a vibrating platform is not a trivial problem, and it generally leads to chaotic behavior.^{58–60} For this study, we have used DEM simulation to predict average bouncing characteristics as a function of vibration parameters (see [Note S1](#)). These models produced a time-averaged bounce height of the sphere $\langle h \rangle$ as a function of dimensionless amplitude and frequency that can be estimated with

$$\frac{\langle h \rangle}{l} = 7.5 \left(\frac{2A}{l} \right)^2 \left(f \sqrt{\frac{l}{2g}} \right)^{2.1}, \quad (\text{Equation 1})$$

where l is the diameter of the sphere, g is gravitational acceleration, A is vibration amplitude, and f is vibration frequency. We also computed the average bounce duration of the bouncing sphere $\langle t \rangle$ as a function of dimensionless amplitude and frequency (see [Figure S1F](#)). Likewise, the average bounce duration can be estimated with

$$\langle t \rangle \sqrt{\frac{2g}{l}} = 1.4 \left(\frac{2A}{l} \right)^{0.21} \left(f \sqrt{\frac{l}{2g}} \right)^{0.29}. \quad (\text{Equation 2})$$

We also assessed the non-dimensionalized average bounce height and duration as a function of the dimensionless relative acceleration (T) of the platform (see [Figures S1G](#) and [S1H](#)). The fitted curves to these two datasets show that the R -square for bounce height and duration versus T is 0.92 and 0.62. These values are much lower than the R -square of fitted surfaces (see [Figures S1E](#) and [S1F](#)), showing that bounce height and duration cannot be predicted by relative acceleration only. The contributions of amplitude and frequency must therefore be considered individually in the context of a vibration-induced assembly.

Rotation model

In addition to bouncing, the assembly process and [Figure 2](#) suggest that the rotation of individual cubes is also an effective packing and assembly mechanism allowing cubes to better fill available vacancies as well as promoting interactions among cubes. To explore this mechanism, we used a $4.8 \times 4.8 \times 4.8$ mm single-cube DEM model with an initial rotation angle (θ) at the corner of a 10° tilted rigid platform ([Figure 5A](#)). The system was subject to gravity and to a sinusoidal displacement applied vertically to the rigid platform. Before applying vibration, the rotated cube initially was in a static equilibrium condition due to friction with

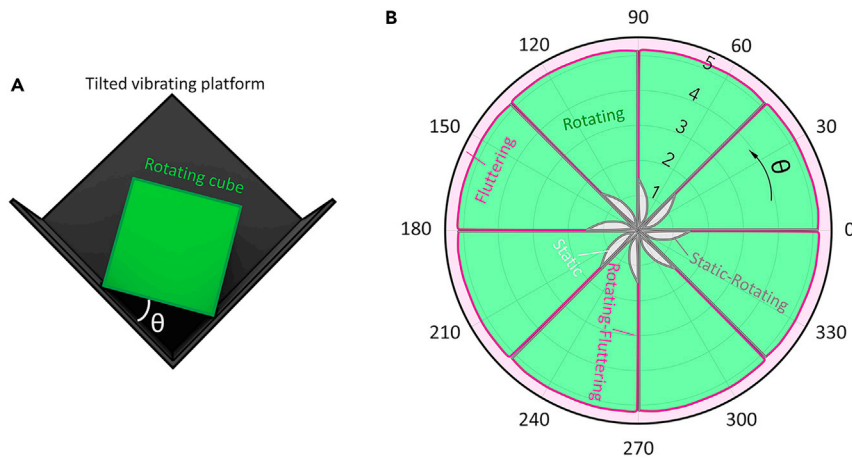


Figure 5. Rotation of single cubical grain as a function of different vibration parameters
 (A) Schematic of the single-cube DEM model rotating due to the vibration of the rigid platform; θ is the initial cube rotation angle; (B) cube rotation map as a function of dimensionless relative acceleration and its initial rotation angle. The rotation map shows the three main regimes: static; rotating; and fluttering regimes.

the walls. This condition duplicates a local configuration where a cube is in contact with its neighbors (or with the assembly platform) but where it is jammed in a mis-rotated position. Our objective was to capture the conditions in which individual cubes rotate from a static equilibrium condition to properly align and assemble. These rotation-based mechanisms can be assessed as a function of initial rotation angle, friction, amplitude, and frequency using the single-cube model. We ran 9,000 models for different combinations of these parameters. Each simulation captured 5 s of physical interactions between the cube and the corner walls—enough time to capture the rotation of the cube for any applied amplitude-frequency response of the rigid platform. Since there were many parameters and combinations, we used the actual physical parameters that were experimentally measured on calcium sulfate cubes. Figure 5B shows the result, in the form of a rose plot showing the state of the cube (static, rotating to assemble, or fluttering) as a function of I and the initial mis-rotation angle of the cube θ . At low I magnitudes and/or high initial mis-rotation angles (θ), the cube did not rotate (static). At higher I magnitudes and/or lower initial mis-rotation angles, the cube rotated (rotating). At high I magnitudes, the system entered a fluttering regime. The rose plot displayed a rotation symmetry that reflects the symmetry of the cube. While the transition from static to rotating depended on the mis-rotation angle of the cube θ , the rotating-fluttering transition only depended on I . From these DEM results, the static-rotating transition can be fitted with Equation 3 at $\theta = 45^\circ$, which is the least favorable initial angle to assembly.

$$\frac{A}{I} = 0.015 \left(f \sqrt{\frac{I}{2g}} \right)^{-0.94} \quad (\text{Equation 3})$$

The rotating-fluttering transition at $\theta = 45^\circ$ can be captured with

$$\frac{A}{I} = 0.035 \left(f \sqrt{\frac{I}{2g}} \right)^{-1.03} \quad (\text{Equation 4})$$

Equations 3 and 4 are compared with the many-cube experiments in the next section.

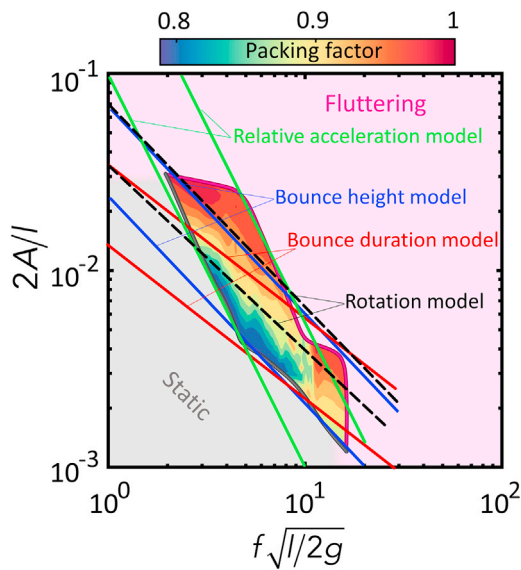


Figure 6. Comparison between experimental phase transition boundaries (i.e., static-packing and packing-fluttering) and packing regime with relative acceleration, bounce height, bounce duration, and rotation models

Predicting many-cube transition lines with single-grain models

Figure 6 shows the experimental assembly map presented in Figure 3 with the addition of the four models described above (relative acceleration, bounce height, bounce duration, and rotation). The relative acceleration model properly captured the upper side (high amplitudes) of the static-packing boundary, but not the lower side (low amplitudes). The bounce height model has the advantage to be a phenomenological model based on grain motion. This model captured the lower side of both the static-packing and packing-fluttering transitions, but it shows some discrepancies with the upper side of these boundaries. The bounce duration model produced predictions with the largest errors, which suggest that bounce duration is not an effective metrics for phase transition and packing. Finally, the rotation model could capture some of the lower sections of the phase transitions but was less accurate for the upper sections. However, considering that this model has no fitting parameter, rotation captures the overall transitions reasonably well. In addition, the overlap between rotation and bounce height model in high packing factor regions suggests that both rotation and bouncing are the key mechanisms for vibration-driven assembly.

In summary, the relative acceleration model and the bounce-height model could properly capture the slope of phase transitions, but their main weakness is that empirical parameters must be used to fit the experiments. The rotation model captures the phase transitions relatively well, with the main advantage to be a purely phenomenological model.

CONCLUSIONS

In this study, we used vibrations and gravity to assemble hard cubes into free-standing crystalline monolayers. The assembly map of these cubes was experimentally and numerically characterized into three regimes and two phase transitions. We complemented these experiments with DEM models to explore in more detail the mechanisms governing the packing and phase transitions of cubes. Our main conclusions are as follows:

- Polyhedral grains can be self-crystallized and/or assembled into large panels.

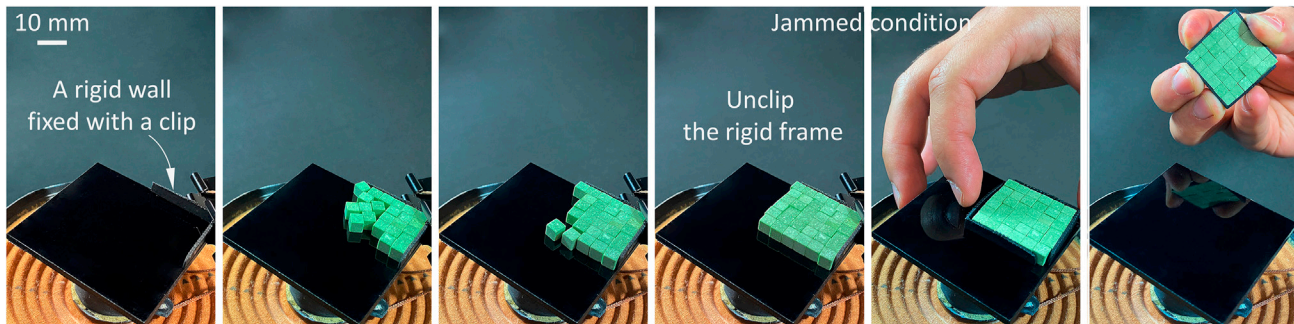


Figure 7. The self-crystallization and/or assembly process of hard cubes into dense free-standing monolayer as a large-piece material and/or structure

- The maximum relative acceleration is not a sufficient parameter to characterize mechanical excitation in the vibration-driven assembly of grains. The contributions of vibration amplitude and frequency must be considered independently.
- The phase transitions followed two distinctive slopes and mechanisms. A part of the static-packing boundary was best captured by the relative acceleration model, while the remaining transitions were better captured by the bounce-height model. The relative acceleration model captured some regions of packing-fluttering, and the other regions in this boundary were partially captured through the bounce-height and/or rotation model. Both of these models involve a fitting parameter.
- The individual-cube-rotation model captures the onset of frictional rotation and fluttering. It is a phenomenological model that captures the overall phase transition relatively well.
- The phase transition can be described by the combination of grain mechanisms and vibration parameters (bouncing mechanism and relative acceleration); however, packing was driven by the grain mechanisms (bouncing and/or rotating) only.
- We experimentally and numerically demonstrated that, within the packing region, optimum packing occurred near the packing-to-fluttering transition.

Vibration-induced fabrication and/or assembly configuration is an efficient procedure to study physics and mechanics underlying athermal far-from-equilibrium systems as well as other fabrication processes, such as freeze casting. In addition, it could offer new routes enabling scalable, rapid, and low-energy fabrication of dense architected materials and/or structures in different environments and atmospheres, for example, topologically interlocked materials (TIMs).^{10–17,61,62} For instance, [Figure 7](#) shows that the self-assembled and/or crystallized cubes can be released from the assembly platform and used as a dense architected panel. The vibration-induced assembly method in this study can also be used to generate anisotropic and/or hybrid TIMs using building blocks with different material properties and/or with slight statistical variations in their geometry (the assembly of more complex shapes is currently under investigation).⁶³ In addition, TIMs tolerate local failures and remain stable when they miss several building blocks. These missed building blocks can be replaced, and the material and/or structure can be healed using the self-assembly technique proposed in this study.

EXPERIMENTAL PROCEDURES

Resource availability

Lead contact

Further information and requests for resources should be directed to the lead contact, Prof. Francois Barthelet, via francois.barthelet@colorado.edu.

Materials availability

No new or unique chemicals were used or generated in this study.

Data and code availability

All codes and computations were implemented with commercial software MATLAB and open-source DEM workbench Granoo; no new computational tools were developed. All data needed for the conclusions in the paper are present in the article and the supplemental information. Additional data related to this work are available upon request to the lead contact author.

SUPPLEMENTAL INFORMATION

Supplemental information can be found online at <https://doi.org/10.1016/j.matt.2022.01.002>.

ACKNOWLEDGMENTS

This work was supported by a Discovery Grant from the Natural Sciences and Engineering Research Council of Canada. A.B. was partially supported by a McGill Engineering Doctoral Award.

AUTHOR CONTRIBUTIONS

Conceptualization, A.B., J.W.P., F.H., and F.B.; methodology, A.B., J.W.P., F.H., and F.B.; software, A.B., J.W.P., and F.H.; validation, A.B., J.W.P., F.H., and F.B.; formal analysis, A.B., J.W.P., and F.H.; investigation, A.B., J.W.P., F.H., and F.B.; resources, F.B.; writing – original draft, A.B., J.W.P., and F.H.; writing – review & editing, F.B.; visualization, A.B.; supervision, F.B.; project administration, F.B.; funding acquisition, F.B.

DECLARATION OF INTERESTS

The authors declare no competing interests.

Received: October 6, 2021

Revised: December 7, 2021

Accepted: January 3, 2022

Published: January 31, 2022

REFERENCES

1. Studart, A.R. (2016). Additive manufacturing of biologically-inspired materials. *Chem. Soc. Rev.* 45, 359–376.
2. Mirkhalaf, M., and Zreiqat, H. (2020). Fabrication and mechanics of bioinspired materials with dense architectures: current status and future perspectives. *JOM* 72, 1458–1476.
3. Behera, R.P., and Le Ferrand, H. (2021). Impact-resistant materials inspired by the mantis shrimp's dactyl club. *Matter* 4, 2831–2849.
4. Bouville, F., Maire, E., Meille, S., Van de Moortèle, B., Stevenson, A.J., and Deville, S. (2014). Strong, tough and stiff bioinspired ceramics from brittle constituents. *Nat. Mater.* 13, 508–514.
5. Nelson, I., and Naleway, S.E. (2019). Intrinsic and extrinsic control of freeze casting. *J. Mater. Res. Technol.* 8, 2372–2385.
6. Mirkhalaf, M., Dastjerdi, A.K., and Barthelat, F. (2014). Overcoming the brittleness of glass through bio-inspiration and micro-architecture. *Nat. Commun* 5, 1–9.
7. Yin, Z., Hannard, F., and Barthelat, F. (2019). Impact-resistant nacre-like transparent materials. *Science* 364, 1260–1263.
8. Amini, A., Khavari, A., Barthelat, F., and Ehrlicher, A.J. (2021). Centrifugation and index matching yield a strong and transparent bioinspired nacreous composite. *Science* 373, 1229–1234.
9. Barthelat, F. (2015). Architected materials in engineering and biology: fabrication, structure, mechanics and performance. *Int Mater Rev* 60, 413–430.
10. Dyskin, A.V., Estrin, Y., Kanel-Belov, A.J., and Pasternak, E. (2001). A new concept in design of materials and structures: assemblies of interlocked tetrahedron-shaped elements. *Scr. Mater* 44, 2689–2694.
11. Mirkhalaf, M., Tanguay, J., and Barthelat, F. (2016). Carving 3D architectures within glass: Exploring new strategies to transform the mechanics and performance of materials. *Extreme Mech. Lett.* 7, 104–113.
12. Mirkhalaf, M., Zhou, T., and Barthelat, F. (2018). Simultaneous improvements of strength and toughness in topologically interlocked ceramics. *Proc. Natl. Acad. Sci. U S A* 115, 9128–9133.
13. Wang, Y., Li, L., Hofmann, D., Andrade, J.E., and Daraio, C. (2021). Structured fabrics with tunable mechanical properties. *Nature* 596, 238–243.
14. Dalaq, A.S., and Barthelat, F. (2020). Manipulating the geometry of architected beams for maximum toughness and strength. *Mater. Des.* 194, 108889.

15. Mirkhalaf, M., Sunesara, A., Ashrafi, B., and Barthelat, F. (2019). Toughness by segmentation: fabrication, testing and micromechanics of architected ceramic panels for impact applications. *Int. J. Sol Struct.* *158*, 52–65.
16. Djumas, L., Simon, G.P., Estrin, Y., and Molotnikov, A. (2017). Deformation mechanics of non-planar topologically interlocked assemblies with structural hierarchy and varying geometry. *Sci. Rep.* *7*, 1–11.
17. Williams, A., and Siegmund, T. (2021). Mechanics of topologically interlocked material systems under point load: Archimedean and Laves tiling. *Int. J. Mech. Sci.* *190*, 106016.
18. Zavattieri, P.D. (2020). Tango with the Piranhas. *Matter* *2*, 23–25.
19. Siegmund, T., Barthelat, F., Cipra, R., Habtour, E., and Riddick, J. (2016). Manufacture and mechanics of topologically interlocked material assemblies. *Appl. Mech. Rev.* *68*, 0408031–04080315.
20. Smeets, B., Pešek, J., Deckers, T., Hall, G.N., Cuvelier, M., Ongenaes, S., and Ramon, H. (2020). Compaction dynamics during progenitor cell self-assembly reveal granular mechanics. *Matter* *2*, 1283–1295.
21. Feng, L., Wang, K.Y., Powell, J., and Zhou, H.C. (2019). Controllable synthesis of metal-organic frameworks and their hierarchical assemblies. *Matter* *1*, 801–824.
22. Lipton, J., Weng, G.M., Röhr, J.A., Wang, H., and Taylor, A.D. (2020). Layer-by-layer assembly of two-dimensional materials: meticulous control on the nanoscale. *Matter* *2*, 1148–1165.
23. Lv, Z., Xing, X., Huang, S., Wang, Y., Chen, Z., Gong, Y., and Han, S.T. (2021). Self-assembling crystalline peptide microrod for neuromorphic function implementation. *Matter* *4*, 1702–1719.
24. Liu, D., Aleisa, R., Cai, Z., Li, Y., and Yin, Y. (2021). Self-assembly of superstructures at all scales. *Matter* *4*, 927–941.
25. Manoharan, V.N. (2015). Colloidal matter: packing, geometry, and entropy. *Science* *349*, 12537511–12537518.
26. Manoharan, V.N., Elsesser, M.T., and Pine, D.J. (2003). Dense packing and symmetry in small clusters of microspheres. *Science* *301*, 483–487.
27. Meng, G., Arkus, N., Brenner, M.P., and Manoharan, V.N. (2010). The free-energy landscape of clusters of attractive hard spheres. *Science* *327*, 560–563.
28. Kraft, D.J., Ni, R., Smallenburg, F., Hermes, M., Yoon, K., Weitz, D.A., and Kegel, W.K. (2012). Surface roughness directed self-assembly of patchy particles into colloidal micelles. *Proc. Natl. Acad. Sci. U S A* *109*, 10787–10792.
29. Sacanna, S., Irvine, W.T., Chaikin, P.M., and Pine, D.J. (2010). Lock and key colloids. *Nature* *464*, 575–578.
30. Smallenburg, F., Filion, L., Marechal, M., and Dijkstra, M. (2012). Vacancy-stabilized crystalline order in hard cubes. *Proc. Natl. Acad. Sci. U S A* *109*, 17886–17890.
31. Thapar, V., Hanrath, T., and Escobedo, F.A. (2015). Entropic self-assembly of freely rotating polyhedral particles confined to a flat interface. *Soft Matter* *11*, 1481–1491.
32. Damasceno, P.F., Engel, M., and Glotzer, S.C. (2012). Predictive self-assembly of polyhedra into complex structures. *Science* *337*, 453–457.
33. van Anders, G., Klotsa, D., Ahmed, N.K., Engel, M., and Glotzer, S.C. (2014). Understanding shape entropy through local dense packing. *Proc. Natl. Acad. Sci. U S A* *111*, E4812–E4821.
34. Jaeger, H.M. (2015). Celebrating soft matter's 10th anniversary: toward jamming by design. *Soft Matter* *11*, 12–27.
35. Richard, P., Nicodemi, M., Delannay, R., Ribiere, P., and Bideau, D. (2005). Slow relaxation and compaction of granular systems. *Nat. Mater.* *4*, 121–128.
36. Lim, M.X., Souslov, A., Vitelli, V., and Jaeger, H.M. (2019). Cluster formation by acoustic forces and active fluctuations in levitated granular matter. *Nat. Phys.* *15*, 460–464.
37. Baker, J., and Kudrolli, A. (2010). Maximum and minimum stable random packings of platonic solids. *Phys. Rev. E* *82*, 061304.
38. Götz, M., Fey, T., and Greil, P. (2012). Vibration assisted self-assembly processing of ceramic-based composites with modular meta-structure. *J. Am. Ceram. Soc.* *95*, 95–101.
39. Lim, M.X., Murphy, K.A., and Jaeger, H.M. (2019). Edges control clustering in levitated granular matter. *Granular Matter* *21*, 77.
40. Neudecker, M., Ulrich, S., Herminghaus, S., and Schröter, M. (2013). Jammed frictional tetrahedra are hyperstatic. *Phys. Rev. Lett.* *111*, 028001.
41. Asencio, K., Acevedo, M., Zuriguel, I., and Maza, D. (2017). Experimental study of ordering of hard cubes by shearing. *Phys. Rev. Lett.* *119*, 228002.
42. An, X.Z., Yang, R.Y., Dong, K.J., Zou, R.P., and Yu, A.B. (2005). Micromechanical simulation and analysis of one-dimensional vibratory sphere packing. *Phys. Rev. Lett.* *95*, 205502.
43. Philippe, P., and Bideau, D. (2003). Granular medium under vertical tapping: Change of compaction and convection dynamics around the liftoff threshold. *Phys. Rev. Lett.* *91*, 104302.
44. Amirifar, R., Dong, K., Zeng, Q., and An, X. (2018). Self-assembly of granular spheres under one-dimensional vibration. *Soft Matter* *14*, 9856–9869.
45. Amirifar, R., Dong, K., Zeng, Q., and An, X. (2019). Bimodal self-assembly of granular spheres under vertical vibration. *Soft Matter* *15*, 5933–5944.
46. Ramaioli, M., Pournin, L., and Liebling, T.M. (2007). Vertical ordering of rods under vertical vibration. *Phys. Rev. E* *76*, 021304.
47. Jaoshvili, A., Esakia, A., Porrati, M., and Chaikin, P.M. (2010). Experiments on the random packing of tetrahedral dice. *Phys. Rev. Lett.* *104*, 185501.
48. Valashani, S.M.M., Barrett, C.J., and Barthelat, F. (2015). Self-assembly of microscopic tablets within polymeric thin films: a possible pathway towards new hybrid materials. *RSC Adv* *5*, 4780–4787.
49. Nowak, E.R., Knight, J.B., Ben-Naim, E., Jaeger, H.M., and Nagel, S.R. (1998). Density fluctuations in vibrated granular materials. *Phys. Rev. E* *57*, 1971.
50. Knight, J.B., Fandrich, C.G., Lau, C.N., Jaeger, H.M., and Nagel, S.R. (1995). Density relaxation in a vibrated granular material. *Phys. Rev. E* *51*, 3957.
51. Cavelier, S., Mirmohammadi, S.A., and Barthelat, F. (2021). Titanium mesh-reinforced calcium sulfate for structural bone grafts. *J. Mech. Behav. Biomed. Mater.* *118*, 104461.
52. Johnson, K.L., and Johnson, K.L. (1987). *Contact Mechanics* (Cambridge university press), pp. 340–373.
53. André, D., Charles, J.L., Iordanoff, I., and Néauport, J. (2014). The GranOO workbench, a new tool for developing discrete element simulations, and its application to tribological problems. *Adv. Eng. Softw.* *74*, 40–48.
54. André, D., Charles, J.L., and Iordanoff, I. (2015). 3D Discrete Element Workbench for Highly Dynamic Thermo-Mechanical Analysis: GranOO (John Wiley & Sons), pp. 82–99.
55. André, D., Girardot, J., and Hubert, C. (2019). A novel DEM approach for modeling brittle elastic media based on distinct lattice spring model. *Comput. Methods Appl. Mech. Eng.* *350*, 100–122.
56. Bergen, G.V.D. (1999). A fast and robust GJK implementation for collision detection of convex objects. *J. Graph. Tools* *4*, 7–25.
57. Farkas, N., and Ramsier, R.D. (2006). Measurement of coefficient of restitution made easy. *Phys. Educ.* *41*, 73.
58. Barroso, J.J., Carneiro, M.V., and Macau, E.E. (2009). Bouncing ball problem: stability of the periodic modes. *Phys. Rev. E* *79*, 026206.
59. Jiang, Z.H., Liang, Z.J., Wu, A.C., and Zheng, R.H. (2018). Effect of collision duration on the chaotic dynamics of a ball bouncing on a vertically vibrating plate. *Phys. A: Stat. Mech. Appl.* *494*, 380–388.
60. Leine, R.I., and Heimsch, T.F. (2012). Global uniform asymptotic attractive stability of the non-autonomous bouncing ball system. *Phys. D: Nonlinear Phenom.* *241*, 2029–2041.
61. Y. Estrin, Y. Bréchet, J. Dunlop, and P. Fratzl, eds. (2019). In *Architected Materials in Nature and Engineering: Archimats, Vol 282* (Springer), pp. 23–44.
62. Estrin, Y., Beygelzimer, Y., Kulagin, R., Gumbsch, P., Fratzl, P., Zhu, Y., and Hahn, H. (2021). Architecturing materials at mesoscale: some current trends. *Mater. Res. Lett.* *9*, 399–421.
63. Kim, D.Y., and Siegmund, T. (2021). Mechanics and design of topologically interlocked irregular quadrilateral tessellations. *Mater Des.* *110155*.

Matter, Volume 5

Supplemental information

**Vibration-driven fabrication
of dense architected panels**

Aram Bahmani, J. William Pro, Florent Hannard, and Francois Barthelat

note S1, bouncing of individual grains

We considered a single-sphere bouncing on a harmonic vibrating rigid platform (Figure. S1A) to predict the bouncing height and bouncing duration, and to explore how they are governed by vibration parameters and other key properties. We used a spherical geometry because the cube itself can create more nonlinearities and obscure the effect of physical parameters due to its angular features and harder to predict bouncing directions. The bouncing of a sphere on a vibrating substrate is a seemingly simple problem, but in fact, it is a complex and difficult phenomenon that generally leads to chaotic behavior¹⁻³. Here we studied this phenomenon using the discrete element method to be consistent with the other modeling approaches. More than 6000 combinations of sphere contact stiffness, coefficient of restitution, density, and applied amplitude-frequency were examined. The total time in these models was set at five seconds, which was sufficient to measure an average height of the bounce. We used the actual physical parameters that were experimentally measured by a calcium sulfate cube. Figures. S1B-D show the trajectory of the bouncing sphere for different combinations of the relative acceleration $\Gamma = A\omega^2 / g$. For $\Gamma \leq 1$, the sphere bounces a few times and then stays in contact with the platform (Figure. S1B). At higher $\Gamma (\Gamma \geq 1)$, the sphere takes off from the platform in a seemingly periodic fashion (Figure. S1C). At yet even greater platform acceleration ($\Gamma \gg 1$), the sphere enters a chaotic regime of bouncing, which can be characterized as an athermal far-from-equilibrium state (Figure. S1D). These results are consistent with previous models for bouncing objects^{S1-3}. Next, we used these DEM results to compute the dimensionless time-averaged height of the bouncing sphere as function of dimensionless amplitude and frequency (Figure. S1E). A 3D regression in MATLAB was used to fit a surface on these results with the R -square of 0.98. We also computed the average bounce duration of the bouncing sphere as function of dimensionless amplitude and frequency (Figure. S1F). The R -square for obtained equation from 3D regression based on non-dimensionalized average bounce duration was 0.93. In addition, we assessed the non-dimensionalized average bounce height and duration as function of the dimensionless relative acceleration (Γ) of the platform (Figures. S1G and S1H). The fitted curves to these two data sets show that the R -square for bounce height and duration versus Γ was 0.92 and 0.62. These values are much lower than the R -square of fitted surfaces (Figure. S1E and S1F), showing that bounce height and duration cannot be predicted by relative acceleration only. The contribution of amplitude and frequency must be considered separately in the context of a vibration-induced assembly.

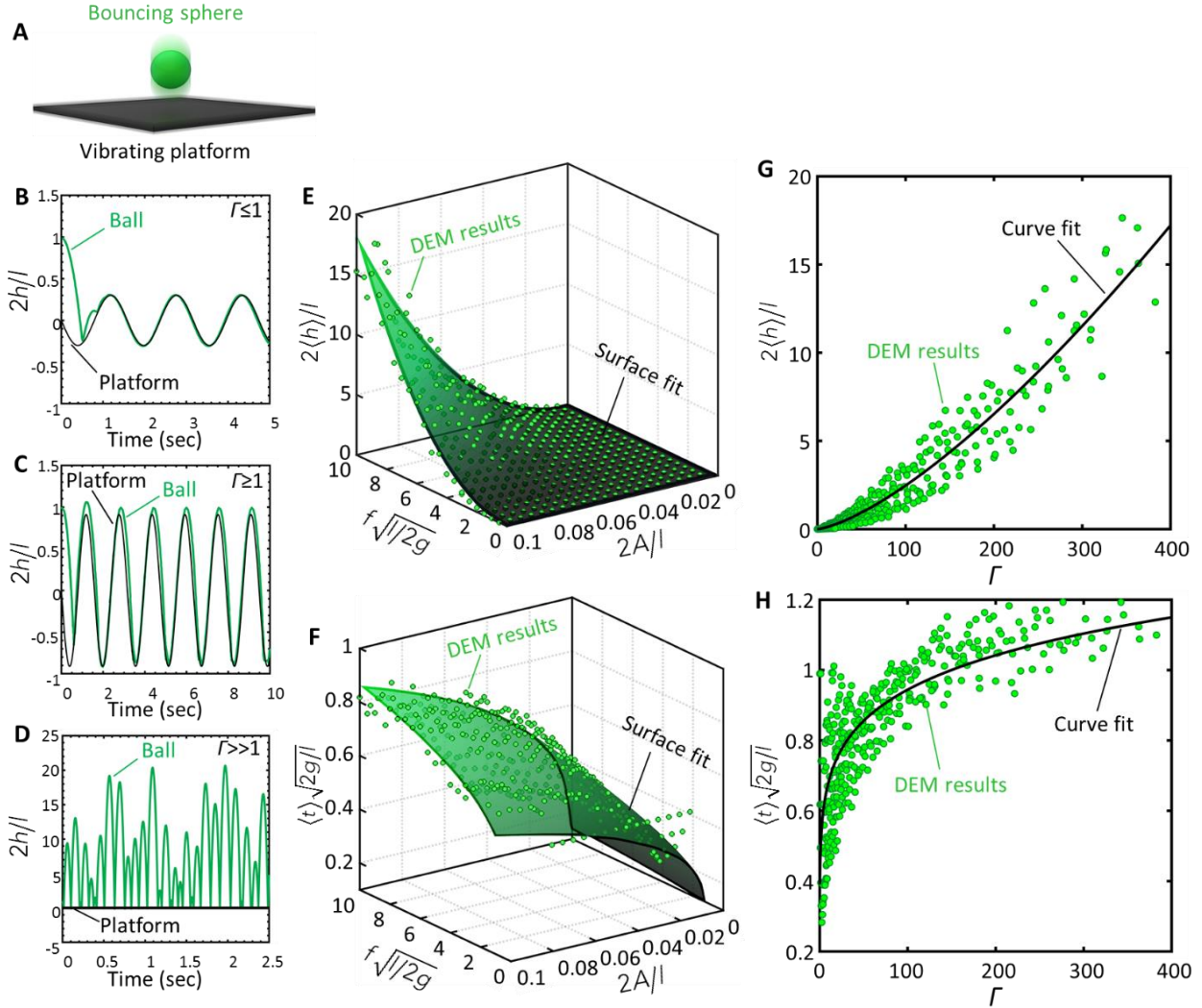


Figure S1. Bouncing of single spherical grain as function of different vibration parameters. (A) Schematic of an individual sphere bouncing on a vibrating rigid platform; (B-D) predictions from the DEM model under various regimes; (E and F) DEM-predicted average bounce height $\langle h \rangle$ and bounce duration $\langle t \rangle$ for the sphere as function of amplitude and frequency with fitted 3D surfaces; (G and H): Bounce height and bounce duration as function of Γ , together with curve fit.

References S1

- S1. Barroso, J. J., Carneiro, M. V., & Macau, E. E. (2009). Bouncing ball problem: stability of the periodic modes. *Phys. Rev. E*, 79, 026206.
- S2. Jiang, Z. H., Liang, Z. J., Wu, A. C., & Zheng, R. H. (2018). Effect of collision duration on the chaotic dynamics of a ball bouncing on a vertically vibrating plate. *Phys. A: Stat. Mech. Appl.*, 494, 380-388.
- S3. Leine, R. I., & Heimsch, T. F. (2012). Global uniform asymptotic attractive stability of the non-autonomous bouncing ball system. *Phys. D: Nonlinear Phenom.*, 241, 2029-2041.